Construction and Building Materials 454 (2024) 138967

Contents lists available at ScienceDirect

Construction and Building Materials

journal homepage: www.elsevier.com/locate/conbuildmat

Spheroidal harmonics for generalizing the morphological decomposition of closed parametric surfaces

Mahmoud Shaqfa, Wim M. van Rees *

Department of Mechanical Engineering, Massachusetts Institute of Technology, Cambridge, MA, USA

ARTICLE INFO

Keywords:
Spheroidal harmonics
Spheroidal coordinates
Spherical harmonics
Customizable parameterization
Conformalized mean curvature flow
Oblate and prolate particles

ABSTRACT

Spherical harmonics (SH) have been extensively used as a basis for analyzing the morphology of particles in granular mechanics. The use of SH is facilitated by mapping the particle coordinates onto a unit sphere, in practice often a straightforward rescaling of the radial coordinate. However, when applied to oblate- or prolate-shaped particles the SH analysis quality degenerates with significant oscillations appearing after the reconstruction. Here, we propose a spheroidal harmonics (SOH) approach for the expansion and reconstruction of prolate and oblate particles. This generalizes the SH approach by providing additional parameters that can be adjusted per particle to minimize geometric distortion, thus increasing the analysis quality. We propose three mapping techniques for handling both star-shaped and non-star-shaped particles onto spheroidal domains. The results demonstrate the ability of the SOH to overcome the shortcomings of SH without requiring computationally expensive solutions or drastic changes to existing codes and processing pipelines.

1. Introduction

Accurate and efficient shape characterization of granular surfaces is crucial in many engineering applications, e.g., interparticle interaction [1], heterogeneous microstructures [2], and fluid flow in granular media, to name just a few. These characterization processes yield shape signatures that can be used for classifying and comparing particulate matter [3], as well as generating virtual microstructures with statistically accurate shapes.

A frequently used approach for shape characterization relies on a harmonic decomposition of surfaces via the spherical harmonics (SH) analysis. The details of SH are well discussed and reviewed in the literature [4,5]. Briefly, to apply the SH analysis, one starts with a parameterization strategy to obtain a bijective mapping of the input mesh onto a unit sphere. This yields the spherical coordinates (θ, ϕ) of each vertex of the input mesh when mapped onto the sphere. A commonly used mapping approach is to normalize the radial distances of each point in the mesh, as computed from the centroid of the surface. The mapping can be used to compute Fourier weights of the mesh by projecting its coordinates onto the SH basis functions, assuming orthonormality. The SH method is commonly used in biomedical applications and medical imaging, e.g., studying the shapes of the human brain [4], heart ventricles [6], and skulls [7]. SH is also used in computer graphics and geometry processing [8] for comparing and classifying objects, as well as in astrophysical [9] and geophysical [10] applications.

In the specific context of particulate and granular mechanics, SH analyses are used to characterize the shape of sand, gravel, and stones as well as to analyze and generate realistic virtual microstructures [2, 11–18]. The surfaces in this domain are mostly (but not exclusively) star-shaped so that an invertible mapping of surface coordinates to the sphere is typically obtained by simply normalizing the radial distance measured from the centroid of the particle surface (this approach is herein referred to as radial mapping). However, applying the SH approach to oblate- and prolate-shaped particles (e.g., river gravel and coral sand, respectively) reveals a visual degradation of the reconstruction quality using SH analysis. Fig. 1, shows a comparison between reconstructing two artificial surfaces: one with an aspect ratio AR = 1 and the same surface but with AR = 2. The reconstruction of the second benchmark shows clear oscillations that take place in regions of large area distortions on the spherical image $\mathbb{S}^2$. Some examples of such oscillations in more practical scenarios are also visible in literature, such as [11] (Fig. 4.10 and 4.12 of that work) and [19]. The degradation appears as high-frequency oscillations in localized regions of the reconstructed surfaces, and are thus difficult to capture with standard second norm errors. Nevertheless, the oscillations have an impact on the spectral properties that in turn affect the measure of the fractal dimension of the particles. Further, in mechanical simulations such as finite or discrete elements, these oscillations can impact the surface contact and the crack propagation along such interface [2,20].

* Corresponding author.
E-mail addresses: mshaqfa@mit.edu (M. Shaqfa), wvanrees@mit.edu (W.M. van Rees).

https://doi.org/10.1016/j.conbuildmat.2024.138967
Received 7 June 2024; Received in revised form 11 October 2024; Accepted 27 October 2024

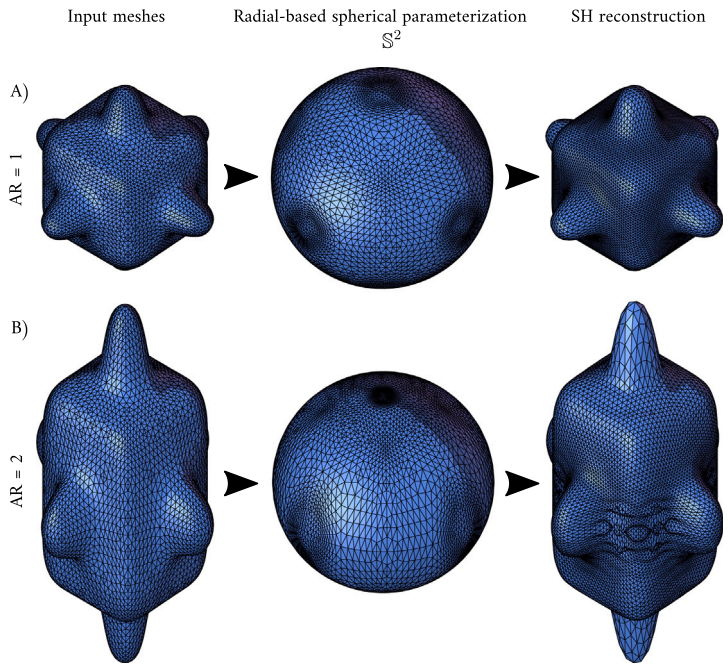

Fig. 1. A benchmark shape [see the online documentation of [21]] analyzed and reconstructed using the radial-based spherical harmonics approach. The top row (A) shows the original benchmark surface with an aspect ratio AR = 1.0, whereas the bottom row (B) repeats the analysis for the same surface stretched to an aspect ratio AR = 2. Each row shows, from left to right, the input meshes, the radial parameterization results, and the reconstruction results. The example shows how changing the AR away from unity distorts the mesh after the mapping, which limits the maximum reconstruction frequency and affects the orthogonality of the bases resulting in oscillations after reconstruction (bottom right).

The appearance of these spurious oscillations on surfaces of low true sphericity index [22] implies that the prevalent radial mapping approach to obtain spherical coordinates induces large topological angle and/or area distortions, which cause discrepancies in the distribution of points on the sphere. Consequently, the orthogonality of the SH basis is increasingly lost [4]. Noisy input data and sharp features in the surface geometry can provide additional sources of surface oscillations in the reconstruction [23–25]. The errors in the reconstruction get worse as the number of analysis degrees increases, demonstrating that this is a divergence issue where Fourier weights do not tend to diminish for high degrees.

These oscillations are sometimes damped using windowing functions, as in e.g. the weighted-SPHARM approach [24]. Such methods, however, introduce new parameters that are not immediately geometrically interpretable while altering all the coefficients without regard to the actual shape of the stone inside the weighting function. The latter means that Fourier weights are changed, such that these cannot be used for the roughness analysis (measure fractals) or to generate representative particles.

Though the radial mapping approach for studying particles is prevalent due to its simplicity and low cost, alternative techniques for mapping surfaces onto spheres exist in other scientific domains. These approaches are often based on the minimization of the conformal energy [26–28] or curvature flow [29–31], and are generally suited to star-shaped as well as non-star-shaped particles. However, the iterative nature of these algorithms can come with a high computational cost, and these approaches still do not completely mitigate the reconstruction problems for prolate/oblate geometries. For instance, conformally mapping a surface onto a sphere can result in large area distortions and large gaps in the distribution of the points. These gaps are limited with bandwidth, so the higher harmonics (frequencies) do not converge at the affected regions [32] which will be a source of oscillations. One possible way to reduce these gaps onto a spherical domain is by balancing the angle and area distortions using local weight functions [33]. For granular surface analysis, however, these alternative techniques to radial mapping have not been widely adopted, possibly due to their computational cost and complexity.

Another possible avenue to mitigate the mapping-induced distortions is to define a parameterization domain that more closely adheres to the dominant geometric features of the considered shapes. Along this line, recent generalizations of the original SH method have taken place to account for open surfaces using the hemispherical harmonics (HSHA) approach [6,34]. This was followed by a more general approach of open surfaces through the spherical cap harmonics (SCHA) [35]. The underpinning idea in the SCHA method is to analyze open surfaces on more general and customizable parameterization domains (i.e., spherical caps prescribed by an opening angle θ_c). More recently, we also proposed a more computationally efficient approach based on the disk harmonics analysis (DHA) to treat nominally flat self-affine rough surfaces [36]. Using such custom parameterization domains in SCHA and DHA to lower mapping-induced topological distortions improves the decomposition and reconstruction results. Recently, Huang et al. [16] attempted to address the oscillation problem by proposing a “shrinkage strategy” to limit the effect of amplified zeroth-order harmonics, effectively parameterizing the radial mapping approach with the particle’s aspect ratio. This procedure resulted in fewer oscillations in the middle band of the particles, though it was still combined with numerical damping of the harmonic basis similar to the weighted-SPHARM approach [24].

Motivated by the success of customizable mapping domains, we propose here to use confocal spheroidal coordinates (oblate and prolate spaces) for the characterization of oblate/prolate granular particles. These domains are customizable in that they contain parameters (the major and minor axes of the spheroid) to be tuned for each particle separately. Formally, they generalize the SH coordinates and contain the SH as a special case. In fact, similar to the SH, the spheroidal basis functions consist of the associated Legendre polynomials with Fourier bases, which makes the transition to spheroidal harmonics seamless for the granular mechanics community. Further, previous experimental work uses spheroids to classify and characterize a wide spectrum of

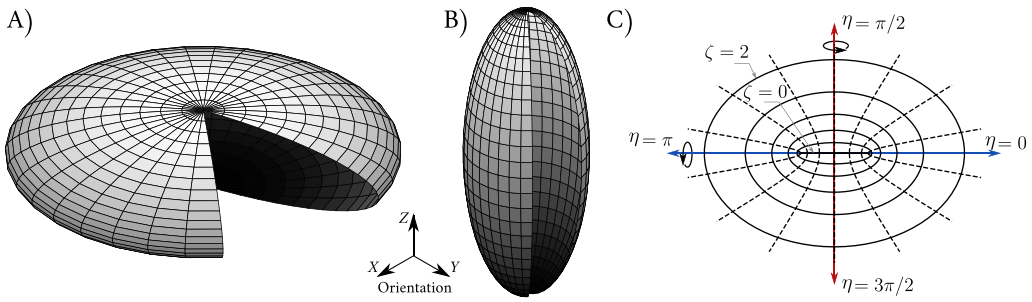

Fig. 2. Oblate (A) and prolate (B) spheroids $\mathcal{E}$ embedded in $\mathbb{R}^3$. (C) The elliptic coordinates where the solid lines represent the confocal ellipses while the dashed lines are the confocal hyperbolas. When the elliptic system revolves about the vertical axis (red) it generates an oblate surface, while the prolate one can be generated by revolving about the horizontal axis (blue). (For interpretation of the references to color in this figure legend, the reader is referred to the web version of this article.)

granular particles [37,38]. This implies that even with a simple low-cost mapping technique such as the radial mapping commonly used in the granular mechanics community, one can expect reduced distortions in this domain.

The rest of this paper is organized as follows. Section 2 introduces the spheroidal coordinate system and the harmonic bases used for the analysis. Section 3 is where we propose methods to determine the spheroidal domains and proper parameterization methods for the analysis of star-shaped (SS) and non-star-shaped (NSS) closed surfaces. Detailed results and comparisons are depicted in Section 4. Eventually, conclusions and future works are summarized in Section 5. For reproducibility, the Python3 codes that were used in this paper are made available on GitHub.

2. Spheroidal space and the corresponding harmonics

2.1. Ellipsoidal and spheroidal coordinates

An ellipsoidal surface in $\mathbb{R}^3$ and centered about the origin $\mathcal{O}$ is written in the Cartesian coordinates as:

$$\frac{x^2}{a^2} + \frac{y^2}{b^2} + \frac{z^2}{c^2} = 1, \tag{1}$$

where a, b, c are positive real numbers that describe the semi-axis lengths along each of the coordinate directions. Spheroidal surfaces form a subset of (1) where $a = b$, and can thus be written as:

$$\mathcal{E} : \frac{x^2 + y^2}{a^2} + \frac{z^2}{c^2} = 1, \tag{2}$$

More generally, in this work, we always interpret a as the repeated semi-axis length and c as the third (non-repeating one), independent of the orientation of the spheroid in $\mathbb{R}^3$. The object is classified as oblate if $a > c$ (Fig. 2A) or as prolate if $c \geq a$ (Fig. 2B). In the latter condition, we intentionally included the sphere ($a = b = c$) because the prolate harmonics mathematically degenerate to the spherical ones as $c \to a$ (as discussed below). Further, we denote the aspect ratio AR $= a/c$ (i.e., $a/c > 1$ is for oblate spheroids, $a/c < 1$ is for prolate ones, and $a/c = 1$ is for a sphere).

Spheroidal coordinates are obtained by revolving elliptic coordinates around an axis. The elliptical coordinates (shown in Fig. 2C) are an orthogonal system formed by confocal ellipses (solid lines) and hyperbolae (dashed lines). Here any elliptical section is identified by $\zeta \in \mathbb{R}^+$, which is analogous to the radial vector in polar coordinates, and the hyperbolic section is identified by the latitude angle η, analogous to the angular coordinate in polar coordinates.

In Fig. 2C, revolving the depicted elliptic coordinates about the horizontal axis generates prolate coordinates, while revolving it about the vertical axis generates oblate ones. The azimuthal angle $\phi \in [0, 2\pi)$ then completes the spheroidal coordinate system (ζ, η, ϕ). Spheroidal coordinates form quadric surfaces of revolution that define a complete set of coordinates to sufficiently describe any point in $\mathbb{R}^3$.

Starting with oblate spheroids, the parametric form of the oblate spheroidal coordinates can be written as:

$$\begin{aligned} x(\zeta, \eta, \phi) &= e\ \cosh\zeta\ \cos\eta\ \cos\phi, \\ y(\zeta, \eta, \phi) &= e\ \cosh\zeta\ \cos\eta\ \sin\phi, \\ z(\zeta, \eta) &= e\ \sinh\zeta\ \sin\eta, \end{aligned} \tag{3}$$

where $(\pm e, 0)$ are the coordinates of the foci along the major axis, and the latitude angle $\eta \in [-\pi/2, \pi/2]$. Similarly, the parametric representation of the prolate coordinates can be written as:

$$\begin{aligned} x(\zeta, \eta, \phi) &= e\ \sinh\zeta\ \sin\eta\ \cos\phi, \\ y(\zeta, \eta, \phi) &= e\ \sinh\zeta\ \sin\eta\ \sin\phi, \\ z(\zeta, \eta) &= e\ \cosh\zeta\ \cos\eta. \end{aligned} \tag{4}$$

For the prolate coordinates the latitude angle $\eta \in [0, \pi]$.

In the context of this paper, we focus primarily on spheroidal surfaces, which are defined by a constant value of $\zeta = \zeta_0$ and parameterized solely through η and ϕ. From the parametric forms in Eq. (3) and (4) we can write the aspect ratio AR of any spheroidal surface as a function of ζ_0, where AR $= [\tanh\zeta_0]^{-1}$ for oblates or AR $= \tanh\zeta_0$ for prolates.

2.2. Spheroidal harmonic functions

The harmonics of oblate and prolate spheroidal coordinates are a special case of the ellipsoidal harmonics, which generalize the spherical harmonics. Similar to the spherical harmonics, the basis can be obtained by assuming that the differential form of the elliptic partial differential equation of Laplace $\nabla^2 f = 0$ is separable, where $\nabla^2 = \Delta$ is the Laplace–Beltrami operator. In this section, we briefly describe the derivation of the bases and introduce our notation to align it with the used SH notation in the granular mechanics literature. Further details can be found in standard textbooks, e.g., [39–43].

2.2.1. Basis functions of oblate coordinates

The Laplacian expression can be simplified by letting $\xi_1 = \sinh\zeta$ and $\xi_2 = \sin\eta$, so that $\xi_1 \in [0, \infty)$ and $\xi_2 \in [-1, 1]$ [40]. By using the identities $\cosh^2 a - \sinh^2 a = 1$ and $\cos^2 b + \sin^2 b = 1$, we can rewrite the parametric coordinates in Eq. (3) as:

$$\begin{aligned} x(\xi_1, \xi_2, \phi) &= e\ \sqrt{(1+\xi_1^2)(1-\xi_2^2)}\ \cos\phi, \\ y(\xi_1, \xi_2, \phi) &= e\ \sqrt{(1+\xi_1^2)(1-\xi_2^2)}\ \sin\phi, \\ z(\xi_1, \xi_2) &= e\ \xi_1\ \xi_2. \end{aligned} \tag{5}$$

After writing the metric coefficients in the curvilinear coordinates, we can write the Laplacian operator in oblate coordinates as:

$$\begin{aligned} \nabla^2 f = &\frac{1}{e^2(\xi_1^2 + \xi_2^2)} \left(\frac{\partial}{\partial \xi_1} \left((\xi_1^2 + 1) \frac{\partial f}{\partial \xi_1} \right) + \frac{\partial}{\partial \xi_2} \left((1 - \xi_2^2) \frac{\partial f}{\partial \xi_2} \right) \right. \\ &\left. + \frac{\xi_1^2 + \xi_2^2}{(\xi_1^2 + 1)(1 - \xi_2^2)} \frac{\partial f^2}{\partial \phi^2} \right). \end{aligned} \tag{6}$$

In our context, we only consider spheroidal surfaces where $\xi_1 = const$, so we drop all the terms related to ξ_1 from the general solution to obtain the Laplace–Beltrami operator on an oblate spheroidal surface.

Classically, the solution of Eq. (6) can be obtained by separation. The general solution form can be written as:

$$f(\eta,\phi) = \Theta\Big(\xi_2(\eta)\Big)\,\Phi(\phi). \tag{7}$$

Substituting the general solution into (6), we obtain two equations. The first is Euler's ordinary differential equation (ODE) as a function of ϕ only:

$$\frac{1}{\Phi}\frac{\partial^2\Phi}{\partial\phi^2} = -m^2, \tag{8}$$

with m^2 is any arbitrary positive number. The second ODE is obtained from applying the separation of variables twice on the general form of Eq. (6) and bundling the rest of the terms as a function of ξ_2 only:

$$\frac{\partial}{\partial\xi_2}\left((1-\xi_2^2)\frac{\partial\Theta}{\partial\xi_2}\right) - \frac{\Theta\, m^2}{1-\xi_2^2} + \Theta\, n(n+1) = 0. \tag{9}$$

Eq. (9) is Legendre's associated differential equation of order m and degree n. Another form of Eq. (9) can be commonly found in the literature by applying the exterior derivative on the first term inside the parenthesis of the left-hand side.

Now, we can write the particular solutions of both ODEs. The solution for Eq. (8) can be expressed via Fourier series:

$$\Phi_m(\phi) = e^{\pm im\phi}, \tag{10}$$

where $i^2 = -1$. Since the solution along ϕ is periodic [with $\Phi_m(\phi) = \Phi_m(\phi + 2\pi)$ and $\Phi'_m(\phi) = \Phi'_m(\phi + 2\pi)$], m must be an integer.

The solution for Eq. (9) can be expressed with the first- and second-kind associated Legendre polynomials, $P_m^n(\xi_2)$ and $Q_m^n(\xi_2)$ respectively. However, here we only use the first kind as the second kind is singular at the poles of the oblate coordinates. From Eq. (9), we write the solution as a function of η:

$$\Theta_m^n = P_m^n(\sin\eta). \tag{11}$$

Now, the particular solution can take the form $f_m^n = P_m^n(\sin\eta)\, e^{im\phi}$ for arbitrary n and $m \in \{-n,\dots,0,\dots,n\}$. The degrees $n \in \mathbb{Z}^+$ represent the ranked roots (eigenvalues) of the associated Legendre polynomials. Subsequently, we can expand a continuous field f distributed uniformly over an oblate as a linear series with weights A_m^n and normalization factors N_m^n:

$$f(\eta,\phi) = \sum_{n=0}^{\infty}\sum_{m=-n}^{n} N_m^n\, A_m^n\, P_m^n(\sin\eta)\, e^{im\phi}. \tag{12}$$

2.2.2. Basis functions of prolate coordinates

As above, let $\xi_1 = \cosh\zeta$ and $\xi_2 = \cos\eta$; with $\xi_1 \in [0,\infty)$ and $\xi_2 \in [-1,1]$. Then, we can rewrite the prolate parametric coordinates in Eq. (4) as:

$$\begin{aligned} x(\xi_1,\xi_2,\phi) &= e\,\sqrt{(\xi_1^2-1)(1-\xi_2^2)}\,\cos\phi,\\ y(\xi_1,\xi_2,\phi) &= e\,\sqrt{(\xi_1^2-1)(1-\xi_2^2)}\,\sin\phi,\\ z(\xi_1,\xi_2) &= e\,\xi_1\,\xi_2. \end{aligned} \tag{13}$$

The corresponding general Laplacian operator of prolate coordinates can be written as:

$$\nabla^2 f = \frac{1}{e^2(\xi_1^2-\xi_2^2)}\left(\frac{\partial}{\partial\xi_1}\left((\xi_1^2-1)\frac{\partial f}{\partial\xi_1}\right) + \frac{\partial}{\partial\xi_2}\left((1-\xi_2^2)\frac{\partial f}{\partial\xi_2}\right) + \frac{\xi_1^2-\xi_2^2}{(\xi_1^2-1)(1-\xi_2^2)}\frac{\partial^2 f}{\partial\phi^2}\right). \tag{14}$$

From Eq. (14) we can see that the general form is similar to Eq. (6) apart from a change in sign in some terms and the definition of ξ_1 and ξ_2. This only changes the particular solution that depends on η, which now becomes:

$$\Theta_m^n = P_m^n(\cos\eta). \tag{15}$$

With this, we can write the expansion of any field f as an infinite series:

$$f(\eta,\phi) = \sum_{n=0}^{\infty}\sum_{m=-n}^{n} N_m^n\, A_m^n\, P_m^n(\cos\eta)\, e^{im\phi}, \tag{16}$$

where m is the order and n is the degree of the solution.

2.2.3. Summary of the spheroidal harmonics

Here we summarize the spheroidal basis for any degree n and order $-n \le m \le n$. The number of evaluated basis functions up to any n-degree is $(n+1)^2$. The normalization factors N_m^n ensure orthonormality of the basis and match the ones derived for the spherical harmonics [42]:

$$N_m^n = \sqrt{\frac{(2n+1)}{4\pi}\,\frac{(n-m)!}{(n+m)!}}. \tag{17}$$

Any function f defined on a spheroidal surface of constant ζ can then be decomposed and approximated as a truncated series up to n_{max} degrees as:

$$\hat{f}(\eta,\phi) = \sum_{n=0}^{n_{max}}\sum_{m=-n}^{n} N_m^n\, A_m^n\, P_m^n\left(\xi_2(\eta)\right)\, e^{im\phi}, \text{ where} \tag{18}$$

$$\xi_2(\eta) = \begin{cases} \sin\eta & a/c > 1 \\ \cos\eta & a/c \le 1. \end{cases} \tag{19}$$

Notice that $\xi_2(\eta)_{oblate} = \xi_2(\eta + \pi/2)_{prolate}$. Numerically, this is equivalent to the spherical harmonics basis but wrapped over a different domain. Due to the truncation error with the infinite series, we used $\hat{f}$ in (18) instead of f such that $\hat{f} \to f$ as $n_{\max} \to \infty$.

To efficiently solve for the Fourier weights A_m^n we refer the readers to the newly proposed approach by Shaqfa et al. [44] through the modified randomized Kaczmarz (RK) algorithms that were accelerated with the conjugate symmetry and sparsity of the signals. Lastly, Fig. 3 visualizes the real part of the harmonics for oblate and prolate basis.

3. Surface parameterization onto spheroidal domains

The surface parameterization bijectively maps surfaces that are embedded in the Cartesian space $\mathbb{R}^3$ onto a target 2-manifold. These mappings are usually not isometric as they do not preserve distances locally. Thus, we can classify mappings into angle-preserving (conformal) and area-preserving mappings. Conformal mapping does not, in general, preserve the local areas of the mapped surfaces which might result in large area distortions. Conversely, area-preserving mapping does not preserve angles. The choice of a suitable mapping is generally application-dependent and keeping a balance between the area- and angle-preserving approaches is often desired [33].

The surface parameterization step is essential to find an equivalent embedding of the surface into the analysis domain. The most common particle-related SH algorithms use radial mapping into a unit sphere, e.g., [11,19]. Although this approach is not guaranteed to be bijective and often induces both angle and area errors, it is simple and numerically efficient, which is important when hundreds of particles are being analyzed in granular mechanics applications.

In this section, we first introduce two possible coordinate inversions from $\mathbb{R}^3$ onto (η,ϕ) that underlie two of the surface parameterizations used in this work. Both inversions are parameterized, and we subsequently discuss the choice of the domain parameters as well as a transformation strategy to register surfaces into a canonical coordinate system. These two parameterizations extend the traditional radial projection in SH, but can only be used for star-shaped (SS) particles (see Section SI-1.1 of the Supplementary Information for a definition). To handle also non-star-shaped (NSS) particles, this section finally discusses a preprocessing step based on the *conformalized mean curvature flow* (cMCF) method [45]. Using this method we can flow particles into NSS particles into SS ones and subsequently use either of the two parameterization techniques.

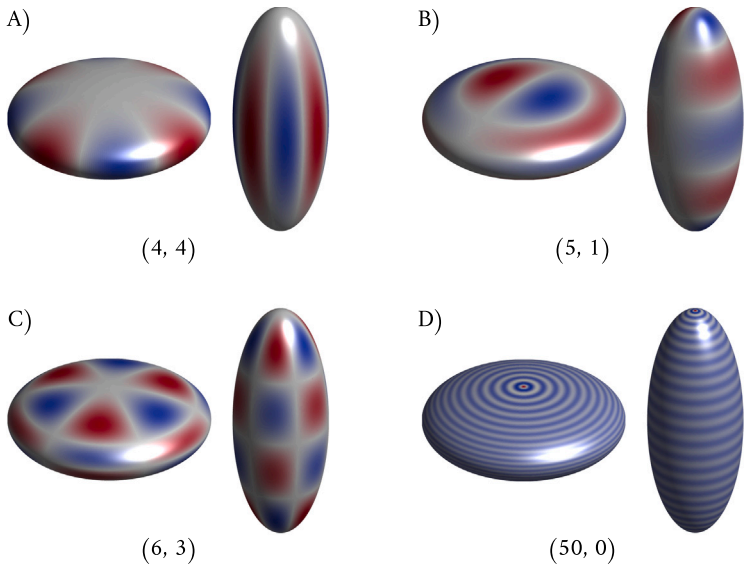

Fig. 3. Examples of the oblate and prolate harmonic basis. (A) → (D) contain oblate (left) and prolate (right) harmonics that correspond for (n, m) pairs (below). To construct the spheroids, we used $\zeta = 0.4$ and $e = 5$. The color represents the normalized real part of the basis $N_m^n \, \Re\{\Theta_m^n(\eta) \, \Phi_m(\phi)\}$. (For interpretation of the references to color in this figure legend, the reader is referred to the web version of this article.)

3.1. Coordinate inversions

The main purpose of this section is to compute the parameterization coordinates in the general solution of Eq. (18); we need to find ϕ- and η-coordinates that correspond to the surface (x, y, z) coordinates. As spheroids are surfaces of revolution (see Fig. 2), computing ϕ is unambiguous and straightforward, such that the inverted azimuthal coordinate $\phi = \tan^{-1}(y/x)$. This definition is similar to the one used for spherical coordinates. For the rest of this section, we only discuss methods to determine the η-coordinate.

First, it is natural to use the curvilinear spheroidal coordinates to define the mapping onto the target spheroids, and we denote this approach the *hyperbolic mapping*. In Section SI-1.2 of the Supplementary Information, we describe the native analytic derivation of the inversion of the curvilinear spheroidal coordinates to compute (ζ, η, ϕ) of a given surface points $\in \mathbb{R}^3$. The analytic coordinate inversions for η, for oblate and prolate spheroids respectively, are given as:

$$\eta = \Im\left\{\cosh^{-1}\left(\frac{\rho_{ob} + iz}{e}\right)\right\}, \quad \zeta = \Re\left\{\cosh^{-1}\left(\frac{\rho_{ob} + iz}{e}\right)\right\}. \tag{20}$$

$$\eta = \Im\left\{\cosh^{-1}\left(\frac{i\rho_{pr} + z}{e}\right)\right\}, \quad \zeta = \Re\left\{\cosh^{-1}\left(\frac{i\rho_{pr} + z}{e}\right)\right\}. \tag{21}$$

Where $\rho = \sqrt{x^2 + y^2}$ is computed for oblate or prolate spheroids as shown in subscripts of ρ in Eq. (20) and (21) respectively. In this inversion, the value of ζ will not affect the hyperbolic coordinate η; the choice of e is the free domain parameter that can be adjusted to each particle individually, as discussed in the next section. This is analogous to spherical harmonics where the value of the radial coordinate r is invariant to the basis functions for surface shape morphology. Further, note that as $e \to 0$, the values of η become equivalent to the polar coordinates θ, and the mapping will reduce to a traditional radial mapping as used in SH.

Fig. 4A shows the hyperbolic mapping in 2D for different choices of the domain parameter e. From the same figure, it can be seen how the distances between the mapped points (red crosses) onto the target ellipse change; thus, directly affecting the distribution of η. The sampling of η is critical to the orthogonality of the basis functions and the overall reconstruction quality as entailed in Eq. (18). In Fig. 4A when $e = 2.5$ the focal points are laid outside the input contour, and as a result, the mapping results have large gaps in the η coordinate (trimmed around the poles). These gaps will result in badly conditioned basis functions that degrade the reconstruction quality. In the next sections, we will describe how to choose the parameter e to avoid this.

Second, we consider a coordinate inversion based on rescaling the conventional spherical coordinates according to a certain chosen aspect ratio, which is the free parameter of this inversion. Rescaling the unit sphere with aspect ratio AR leads to a spheroid of constant $\zeta = \zeta_0$, with $\text{AR} = [\tanh \zeta_0]^{-1}$ for oblates or $\text{AR} = \tanh \zeta_0$ for prolates (where the scaling is independent of e). To compute the coordinate inversion from given particle surface points $\in \mathbb{R}^3$, we then use a standard spherical radial projection to compute an approximation to the latitude angle denoted as $\hat{\eta}$. This simplified radial mapping replaces the exact hyperbolic coordinate η with the approximation:

$$\hat{\eta} = \tan^{-1}\left(\text{AR}\,\frac{z}{\sqrt{x^2 + y^2}}\right). \tag{22}$$

This approximation can be understood mathematically as a linearization (first-order approximation) of an exact spheroidal coordinate η, discarding higher-order terms in the distance from the target surface with ζ_0 and e (a full derivation is shown in Section SI-1.3 of the Supplementary Information). As $\text{AR} \to 1$, this mapping is equivalent to the radial mapping used in SH.

Fig. 4B shows an example of this 2D radial mapping approach onto different elliptic targets for multiple choices of the domain parameter AR. Due to its similarity with the traditional radial mapping in SH, we here refer to it as the radial mapping approach.

3.2. Choice of domain parameters

Here we discuss the choice of the domain parameters e (for the hyperbolic mapping) and AR (for the radial mapping), starting from an arbitrary closed surface with n_p vertices in $\mathbb{R}^3$. First, we discuss a generic transformation to place any particle object in canonical coordinates. Then, we discuss the choice of domain parameters and the details of the mapping for each of the three proposed approaches.

3.2.1. Canonical coordinates

To reduce the dimensionality of the fitting problem and place objects in canonical coordinates, we first translate our object such that the geometrical centroid is placed at the origin $\mathcal{O}$. Next, we rotate the object to align the object axis that maximizes the variance (largest dimension of the object) with the X-axis, while the one with a minimum variance

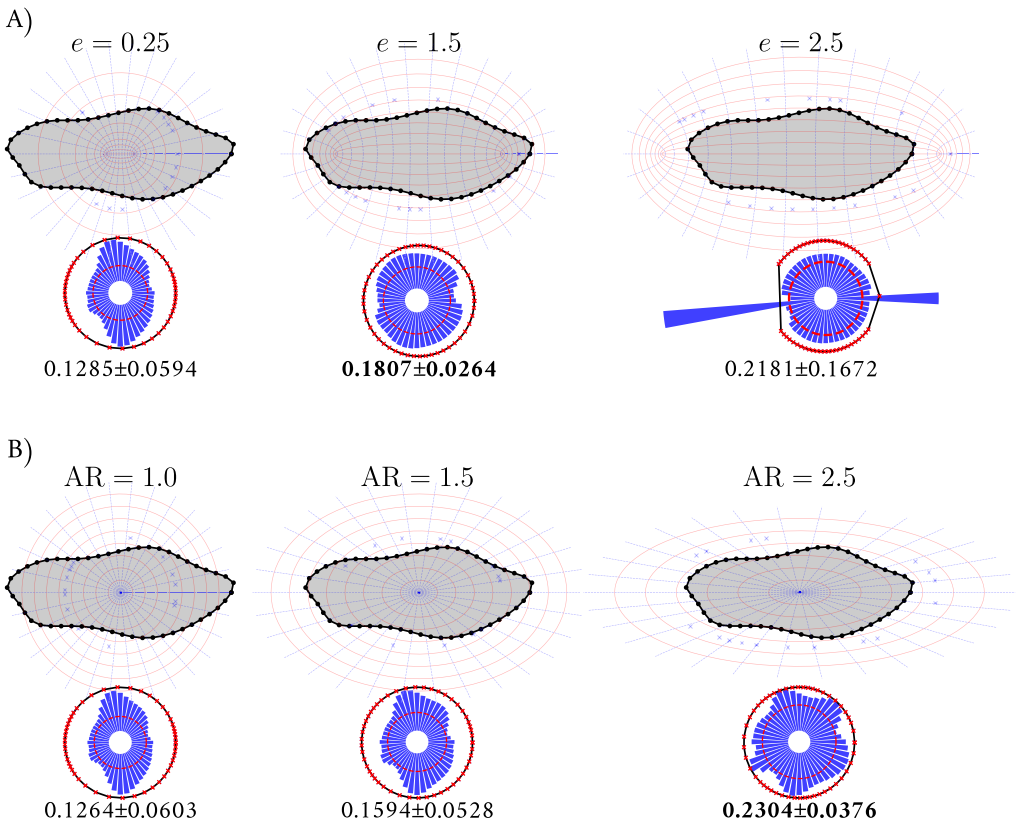

Fig. 4. Computing the mapping of 2D closed contours, constituted by equidistant segments, via two different coordinate inversions. The 2D contours were used to simplify the visualization of the mapping process as a cross-section of a given stone. (A) mapping the 2D contour using hyperbolic mapping onto several target coordinates as a function of the focal distance e. For this set the choice of ζ was arbitrary as the mapping is a function of e only. (B) mapping of the same contour using the rescaled polar coordinates approach as a function of the aspect ratio AR = a/c. The radial bar chart underneath each inset shows the radial distribution of the arclength between two consecutive points onto the target elliptic domain and was annotated with the average ± standard deviation (STD). The confocal red dashed circle in the radial charts marks the corresponding average arclength. Minimal STD (**boldfaced**) of the illustrated examples represents a more uniform mapping that typically corresponds to a better reconstruction accuracy. The mapped points (red crosses), in the lower insets, have been visualized when $\zeta \to \infty$ for the hyperbolic mapping (A), and rescaled circles with AR → 1 for the radial one (B). (For interpretation of the references to color in this figure legend, the reader is referred to the web version of this article.)

is aligned with the Z-axis. One efficient way to do that is by applying the singular value decomposition (SVD) approach to the $3 \times n_p$ vertex matrix P, yielding $P = U\Sigma V^T$ with U is a 3×3 rotation matrix. The canonical placement can then be computed as $\hat{P} = U^T P$. By construction, prolate-like surfaces will have their major axis aligned over the X-axis. So, we rotate prolates by an additional $+\pi/2$ about the Y-axis to align with the basis definition (cf. Fig. 3); this is applied just before the analysis step. By averaging, we merge two of the closest semi-axis lengths into one in order to find initial guesses for semi-axis lengths a and c, based on which we classify whether the surface is oblate or prolate.

After the canonical transformation and spheroidal classification, we can now use a least-squares fit to find the spheroidal parameters a and c that best describe the surface. To this end, we write the general equations for oblate and prolate surfaces *implicitly* as level-set functions:

$$f_{oblate}(x, y, z) = c_1(x^2 + y^2) + c_2 z^2 - 1. \tag{23}$$

$$f_{prolate}(x, y, z) = c_1 x^2 + c_2(y^2 + z^2) - 1. \tag{24}$$

We then find c_1 and c_2 from a least-squares fitting of the appropriate level-set function to the vertex matrix P. Afterward, the spheroidal coordinates can be extracted such that the focal distance $e = \sqrt{|1/c_1 - 1/c_2|}$, while $\zeta = \cosh^{-1}(a/e)$ or $\zeta = \sinh^{-1}(a/e)$ depending on whether the fitted spheroid is oblate or prolate, respectively. After reconstructing our surface with the spheroidal harmonics, we can reverse the rotations and placements removed from the canonical systems to match the registration of the input surface.

3.2.2. Radial mapping onto spheroids for star-shaped (SS) particles

The radial projection approach is straightforward to implement and computationally inexpensive, which explains its intensive use in particulate matter research. For a radial spherical parameterization onto $\mathbb{S}^2$, the radial mapping is obtained by simply normalizing the vectors pointing from the geometric centroid to any point on the surface. Such a normalization process maps all vertices on the surface to a unit sphere. For our parameterized radial map, we set the domain parameter AR directly as the aspect ratio of the fitted canonical spheroid. We note that this combination of radial mapping and spheroidal analysis is equivalent to performing classical spherical harmonics on a *rescaled* version of the granular particle, similar to the approach proposed in [16] (but without their damping of the weights).

To ensure bijectivity, this radial-based mapping method requires that any radial vector pointing out from the geometric centroid intersects only once with the particle surface. In other words, the mapping should be always bijective, meaning that each point on the particle surface corresponds to a unique point on the target spheroid $\mathcal{E}$. If this is the case, the particle is characterized "star-shaped" (SS); otherwise, the particle is characterized "non-star-shaped" (NSS), similar to the use of these terms in SH approaches. Visual examples of SS and NSS particles are discussed in Section SI-1.1 of the Supplementary Information. In this work, we restrict the radial mapping approach described in this section to SS particles only.

3.2.3. Hyperbolic mapping onto spheroids for star-shaped (SS) particles

Following the exact spheroidal coordinate inversion, we can directly obtain η associated with the hyperbolic curve intersecting a given

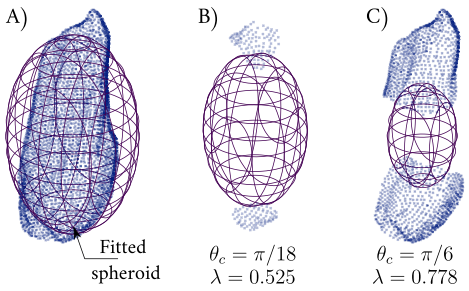

Fig. 5. Comparison between the least-squares fit and the inscribed spheroids as a function of θ_c to find the target spheroid $\mathcal{E}$ for the stone FP_C_684_1 [the stone was retrieved from [46]]. (A) shows the results of the least squares fit with AR = 0.4630 (and the here redundant $e = 0.0805$) (prolate spheroid). (B) is the scaled spheroid results (using $\theta_c = \pi/18$) with an optimal $e_{opt} = 0.0626$. (C) same as (B) but with $\theta_c = \pi/6$ and a corresponding $e_{opt} = 0.0423$.

location in $\mathbb{R}^3$. However, as explained above, the value of η will depend on the choice of the domain parameter e. The examples in Fig. 4A show that the choice of e have a significant impact on the quality of the mapping. Specifically, when the focal points are outside of the convex hull of the surface points, the hyperbolic directors tend to cluster points in the vicinity of the major axes of the spheroid resulting in a trimmed spheroidal domain and often non-bijective images (see Fig. 4A when $e = 2.5$). This results in a faulty reconstruction of the surface.

To find a suitable choice of e for a given particle, we start from the least-squares fit values of a and c and compute an initial guess for $e = \sqrt{|a^2 - c^2|}$. To find out if the value of e extends beyond the particle surface, we define two cones emanating from the centroid to the North and South pole of the registered surface, respectively. Each cone has a user-defined opening angle θ_c. Next, we filter out all the points that do not fall inside this cone, such that $|\theta| \notin (0, \theta_c)$ or $\notin (0, \pi - \theta_c)$ for prolate surfaces and $|\pi/2 - \theta| \notin (0, \theta_c)$ for oblate ones. Here, $\theta = \tan^{-1}\left(z/\sqrt{x^2 + y^2}\right)$ which is measured from the positive Z-axis. The last step is to iteratively shrink the fitted spheroid by shrinking e to λe with $\lambda < 1$ until all the selected points by the cone fall outside the spheroid. Fig. 5 shows a comparison between the fitted target spheroid and the optimized ones as a function of θ_c and their corresponding scales λ. As can be seen from the same figure, the smaller θ_c the larger the target. In general, the reconstruction accuracy favors target spheroids that are as large as the input surfaces to reduce topological distortions. In this work, using $\theta_c = \pi/18$ was satisfactory for the tested oblate and prolate stones.

After finding the optimal e, a particle may or may not be SS, as defined by whether any η coordinate line intersects with the surface more than once. In Section SI-1.1 of the Supplementary Information, we show examples of SS and NSS stones in the context of hyperbolic mappings. In the results below, we only apply the hyperbolic techniques to surfaces for which this results in bijective mappings; those surfaces are typically SS as well.

Overall, the reconstruction results of the herein-proposed optimal target spheroid with hyperbolic mapping were found to be better than using the proposed radial mapping with the fitted spheroid. This is mainly because the hyperbolic directors tend to closely sample points near the high curvature vicinity onto the target spheroids. This near-pole clustering helps in the regularization process and the convergence of the analysis. Further, the hyperbolic mapping tends to result in a more uniform sampling of η, which reduces the orthogonality error of the basis functions. An example illustrating these differences between the two mapping approaches for a 2D problem is given in Section SI-1.4 of the Supplementary Information.

3.2.4. Conformalized mean curvature flow (cMCF) for fairing non-star-shaped (NSS) shapes

Applying radial or hyperbolic mapping to NSS particles onto target spheroids typically results in nonbijective spheroidal images. To enable the ability to analyze NSS particles, we here propose a preprocessing step based on curvature flow iterations, in order to conformally map an NSS particle into an SS image, which enables the use of the radial or hyperbolic maps as proposed above. In general, the curvature flow methods resemble a smoothing (fairing) process that deforms the input surface into a more convex state.

Several flow-based approaches exist for finding conformal mappings onto a target surface. The discrete Ricci flow [29] approach is one of the most commonly used methods, with applications in, for instance, fairing rough surfaces. The Ricci flow however is an intrinsic flow method, so that after the flow reaches the target (user-defined) curvature we need to find the equivalent embedding into $\mathbb{R}^3$. A robust explicit flow alternative, more suitable to our context, is the conformalized mean curvature flow (cMCF) proposed by Kazhdan et al. [45]. This method is a modified version of the original MCF approach for convex surfaces [47]. A further improvement was proposed in [31] to specifically enhance cMCF for surfaces with sharp features. However, the cMCF by [45] was found sufficient for granular mechanics particles and will be briefly discussed below. We implemented the cMCF using the efficient finite element method (FEM) operators provided in [21] that follow the discrete differential geometry operators defined in [48].

Unlike the Ricci flow approach, the cMCF does not flow into a prescribed target metric, instead, it converges into a sphere. Before converging into a sphere, the cMCF flow passes through intermediate diffeomorphism stages (fairing iterations) where the surface becomes star-shaped while the map remains conformal. Note that due to the conformal nature of the map, after many fairing iterations, we can obtain large local area distortions that can harm the surface reconstruction quality. In this work, we therefore generally perform iterations on NSS surfaces until they become star-shaped. After fairing we can apply one of the abovementioned radial or hyperbolic mappings as a complementary step to find the target spheroid of the diffeomorphism. Since the resulting diffeomorphism surfaces are close to being spheroidal in shape, applying the least-squares fitting approach of Section 3.2 leads to a spheroid that is very close to the smoothed surface. In practice, the radial map performed similarly to the hyperbolic map on these smoothed particles. We therefore opt to forego the additional complexity of the hyperbolic mapping and combine the cMCF solely with the simple radial mapping approach in the results presented below.

4. Results and discussions

In this section, we present and discuss the results of the spheroidal harmonic approaches presented in this paper for genus-0 closed particles. We denote the proposed radial mapping in Section 3.2.2 by rSOH and the hyperbolic one in Section 3.2.3 by hSOH, and the cMCF-preprocessed with radial mapping in Section 3.2.4 by c-rSOH. We note that, as discussed above, rSOH and hSOH are only suited for SS particles, whereas the c-rSOH can be applied to both SS and NSS particles.

First, we analyze common particles from the granular mechanics community where surfaces are usually convex or star-shaped (SS). For this, we compare the results of all three proposed approaches for two different datasets. We also compare our results with the traditional SH and show numerical evidence for the superiority of the proposed approaches. Second, we handle non-star-shaped (NSS) particles using the c-rSOH approach only. The datasets that we base our analysis on are summarized as follows:

- The first dataset consists of scanned stone masonry rubble. They were used to construct as-built digital twins for stone walls [49]. The dataset was acquired by a portable laser scanner and can be accessed from Saloustros et al. [46].

- The second dataset is a collection of scanned aggregate particles [50]. It was produced using a novel 3D light scanner. The dataset can be accessed from Thilakarathna [51].
- The third dataset consists of scanned Calcite and Kieselkalk ballast stones that are used as railways ballast rubble [52]. It can be accessed from Suhr et al. [53].

For reproducibility reasons, we base our benchmark surfaces on three datasets that are published online. Moreover, we use the code names of the analyzed particles as given by the original authors of each dataset. For consistency, prior to our analyses, we remeshed all the obtained raw data (point clouds or triangulated surfaces) via the screened Poisson reconstruction approach [54] implemented in the open-source library MeshLab [55]. Moreover, to make triangular meshes Delaunay, we used the edge flipping strategy described in Lawson [56].

4.1. Analysis and reconstruction of star-shaped (SS) stones via c-rSOH, hSOH, and rSOH

We start by studying the SS particles that are included in the first two datasets [46,51]. We analyzed and reconstructed a set of ten stones for each dataset using the radial, hyperbolic, and conformal-preprocessed spheroidal harmonics as well as a traditional spherical harmonics (SH) approach for comparison.

4.1.1. Dataset 1: Stone masonry rubble (SS)

The provided point clouds in the first dataset Saloustros et al. [49] were used for building a digital twin for real stone masonry walls. Such stones are generally sparse and do not give enough details about the roughness and texture of the stones. Consequently, we used only $n_{max} = 20$ degrees for analyzing and reconstructing this dataset. Choosing higher expansion degrees for the particles in this dataset makes the analysis prone to diverge in the regularization step, especially when the mapping domain has large area distortion. As a reconstruction base, for all the proposed approaches, we used an icosahedron mesh subject to three refinement cycles (with 642 vertices and 1280 faces). The icosahedron spheres were rescaled to create a spheroidal base mesh for the reconstruction. This leads to slightly distorted triangles in the base mesh, but we here ignore this error that makes the points slightly nonuniform for the reconstruction basis.

Fig. 6 shows a selected set of reconstruction results that serves as numerical comparisons among the c-rSOH, hSOH, rSOH, and SH approaches. The left column shows the remeshed input meshes from [46]. The next four columns show the results of the (from the left) c-rSOH, hSOH, rSOH, and SH, respectively. For the c-rSOH approach, we only used three fairing iterations ($j = 3$) and a non-dimensional time step $\delta = 0.0005$ with the cMCF method given that this time step is used for scaled diffeomorphisms with a surface area of unity.

We expressed the reconstruction error between the input and reconstructed meshes over a randomly sampled subset of points with the normalized average Hausdorff distance between two aligned and randomly sampled meshes and denoted it by A-RMSE as annotated in Fig. 6. Here and in all results below we normalized A-RMSE with respect to the diagonal length of the bounding box (BB) of the input surface. In the same figure, boldfaced A-RMSE results highlight the best reconstruction results obtained across all the approaches. The rest of the results are shown in Section SI-2.1 of the Supplementary Information.

The A-RMSE results show how the c-rSOH, hSOH, and rSOH outperform the traditional SH. The results obtained by the c-rSOH and hSOH approaches achieved the lowest A-RMSE values, with rather small differences between the proposed approaches for this dataset. The proposed approaches resulted in consistent triangular meshes that are not contracted, overly stretched, or wavy in the middle band of the stones, in contrast to the SH reconstructions shown on the right side of the figures. Notably, the oscillations resulting from SH dilute details in other parts of the stones that are far from the oscillations band (e.g., notice the reconstruction of the lower part of stone FP_C_785_1 in Fig. SI-6).

As discussed in Section 3.2.2, the rSOH approach is AR-dependent. For each of the presented results of rSOH, we used the least-squares fit discussed in Section 3.2 to set the aspect ratio used in the mapping. To study the impact of varying this domain parameter (AR) on the reconstruction accuracy, we manually varied the aspect ratio over a wide range of values and performed the rSOH method for each aspect ratio independently. Fig. 7 depicts the relation between the reconstruction radial root-mean-square error (R-RMSE) as a function of the chosen AR for a specific stone (see section SI-2.2 in the SI for the same analysis performed on other stones in the database). The R-RMSE is defined here as:

$$\text{R-RMSE} = \frac{\sqrt{\sum_{i=1}^{n_v} \left(d_{OV,1}^{(i)} - d_{OV,2}^{(i)} \right)^2 / n_v}}{d_{diag}}, \tag{25}$$

where $d_{OV,1}^{(i)}$ and $d_{OV,2}^{(i)}$ are the radial distances from vertex i to the centroid of each mesh, for the first and second meshes, and d_{diag} is the diagonal length of the parallelepiped bounding box. The R-RMSE measure is used when the number of the vertices of both meshes matches and they are ranked in the same order. From Fig. 7, we can see that the optimal AR value does not exactly coincide with the least-squares fitted AR, though it is very close. This is also true for the other stones in the dataset (section SI-2.2 in the SI), indicating that our fitted AR achieves a near-optimal reconstruction for radially mapped SS particles. Further, note that in all these cases the R-RMSE significantly increases away from its minimum as the AR approaches unity, i.e. when approaching the SH results. Further, note that in all these cases the R-RMSE significantly increases away from its minimum as the AR approaches unity, i.e. when approaching the SH results, emphasizing the benefit of the SOH approach over the traditional SH method.

The inset in Fig. 7 plots the spectrum of shape descriptors for a range of spheroid aspect ratios. Here the radial shape descriptors D_r^2 are defined simply as the unweighted norm of the Fourier weights in the different coordinate directions:

$$D_r(n)^2 = D_x(n)^2 + D_y(n)^2 + D_z(n)^2, \qquad \text{with}$$
$$D_i(n) = \sqrt{\sum_{m=-n}^{n} \|A_{m,i}^n\|^2}, \quad \forall i \in \{x, y, z\}. \tag{26}$$

The plot demonstrates that the spectral properties of the reconstructed shape, as expressed in these shape descriptors, vary depending on the AR. This implies that these descriptors cannot directly be used to compare stones parameterized with different ARs or compute fractal dimensions whenever we use the rSOH approach. Moreover, we see that the tail of the descriptors chart tends to stray away from zero for parameterization with ARs that are far from the optimal one; hence, showing a divergence behavior for the series.

4.1.2. Dataset 2: Aggregate particles (SS)

The second dataset [51] consists of a denser scan of millimeter-sized aggregate particles. These aggregates are typically found in concrete mixes and used in Thilakarathna et al. [50] to generate realistic aggregate particles via the traditional SH approach. As this dataset provides higher frequency content, we used $n_{max} = 30$, apart from the B4 and B7 stones where we used $n_{max} = 20$. For the c-rSOH we used three fairing cycles for all the stones except for B7, which required five iterations to fair into a star-shaped surface. Fig. 8 shows the reconstruction results for all methods considered in this work, using three refinement cycles on an icosahedron as a reconstruction base (with 2562 vertices and 5120 faces). More results on this dataset are shown in Supplementary Information document sections SI-2.1 for the reconstruction examples, and SI-2.2 for the reconstruction quality as a function of selected AR. Similar to the first dataset, the results of the c-rSOH and the hSOH presented the best reconstruction accuracy in

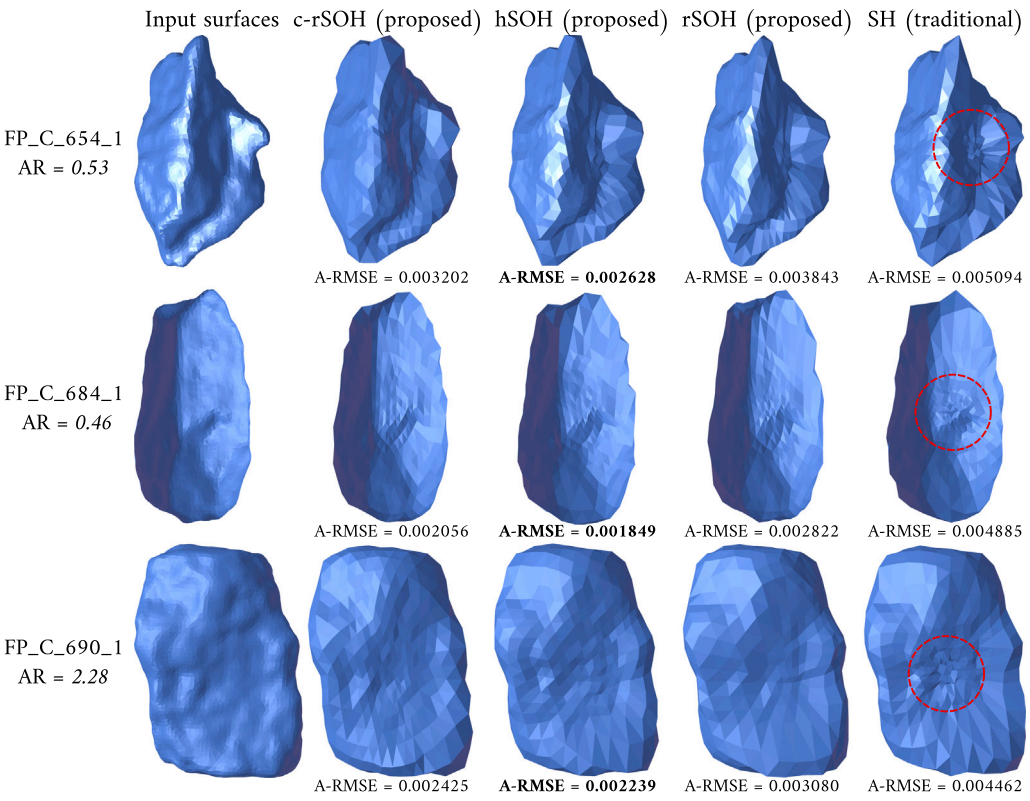

Fig. 6. Reconstruction of a selected set of SS rubble stones [46] via the conformal spheroidal approach (c-rSOH, second column), hyperbolic spheroidal approach (hSOH, third column), radial spheroidal approach (rSOH, fourth column), and traditional spherical harmonics (SH, fifth column). The code names and the fitted aspect ratios (AR) for the stones are shown on the far left annotations. Each reconstructed stone shows the normalized average distances (A-RMSE) below. Boldfaced **A-RMSE** highlights the best reconstruction accuracy.

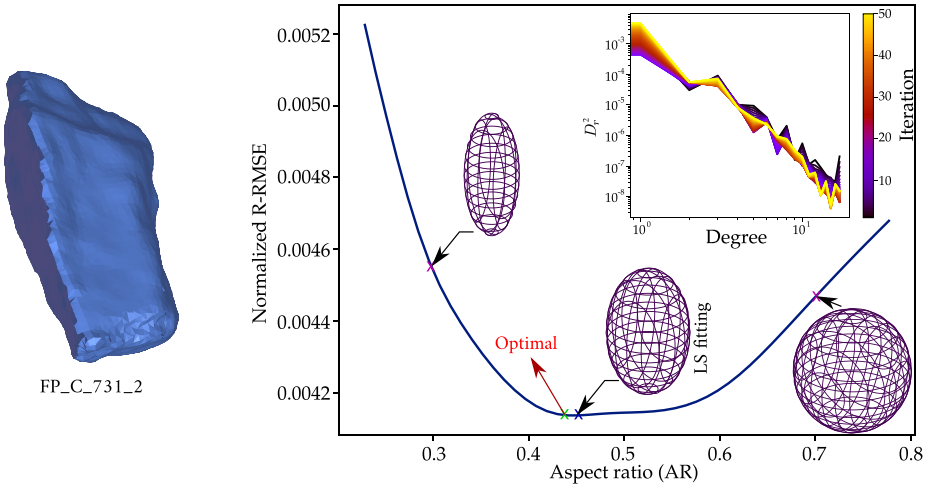

Fig. 7. For stone FP_C_731_2 [46] (shown on the left) we vary the AR of the spheroidal domain, and record the normalized R-RMSE (plotted on the right). The optimal mapping was observed to be when AR = 0.43, while the one obtained from the least-squares fit proposed in Section 3.2 was 0.45. The inset of the plot further shows the variation of the shape descriptors as we change the AR in 50 steps from 0.23 → 0.78. (For interpretation of the references to color in this figure legend, the reader is referred to the web version of this article.)

comparison with rSOH and the traditional SH. Although less than the SH, we see that a few stones constructed with rSOH and hSOH still show some minor oscillations (see also stones B4 and B7 in section SI-2.1 of the Supplementary Information).

For the second dataset, the hSOH significantly outperforms rSOH on the A-RMSE error metric. As the hSOH tends to sample denser near the poles of high curvature than the rSOH, we observed that the hSOH is, in general, more area-preserving than the rSOH.

The problem of the large discrepancy between the surface point cloud and the target spheroid can be completely overcome using the c-rSOH approach. Overall and in global error measures (R-RMSE and A-RMSE), for star-shaped particles the hSOH and rSOH approaches provide improvements over SH with little additional complexity. Out of the two, hSOH generally outperforms rSOH by reducing distortion near regions of high curvature. The c-rSOH is more general and can be used for SS stones as well, but requires additional computation cost

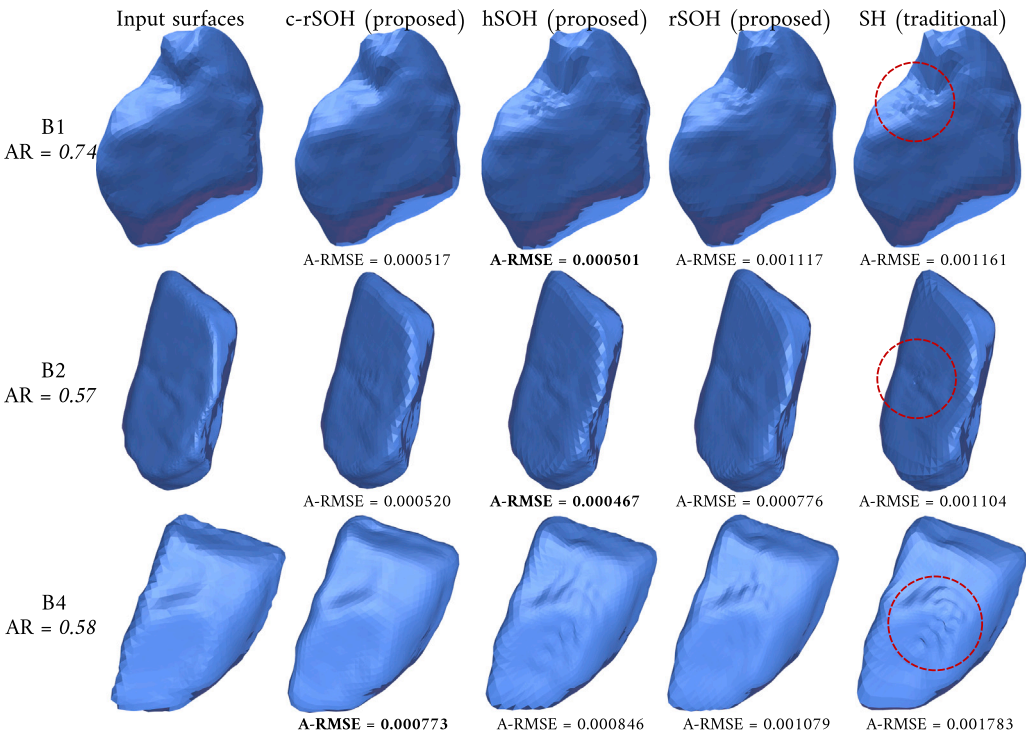

Fig. 8. Reconstruction of a selected set of SS aggregates [51] through the conformal- and radial-based approaches. The first column contains the input surfaces, while the second, third, and fourth are the reconstruction via the spheroidal harmonics c-rSOH, hSOH, and rSOH, respectively, as well as the traditional spherical harmonics (SH) in the fifth column. The left-hand texts show the annotation per stone and the fitted aspect ratio (AR) for the spheroidal coordinates. Each reconstructed stone shows the normalized average distances (A-RMSE) below. Boldfaced **A-RMSE** highlights the best reconstruction accuracy.

while offering relatively little improvement over the other two methods (see Section 4.4).

We generally found that the performance of our newly proposed methods is robust to various choices of morphological metrics. As an illustration, Fig. 9 shows the stone B2 of the second dataset as reconstructed using all four methods considered (for this stone, $n_{\max} = 30$), visualized with two different metrics. The first metric, which we denote H-RMSE, measures the root-mean-square error of the mean curvature h [57]. The second metric, denoted R_n-RMSE, measures the root-mean-square error of the roundness metric R_n proposed in [58]. From the visualizations, we observe that the mean curvature errors are largest near the sharp edges. The c-rSOH method provides the best regularization of the mapped field through the conformal flow and has the smallest curvature errors. On the other hand, the roundness error has only small differences between all three proposed methods, though all three clearly outperform the SH approach. We measured the same error metrics for two other stones in this second dataset, and found in all cases similar trends as reported in this work based on the A-RMSE metric.

4.2. Analysis and reconstruction of non-star-shaped (NSS) stones via c-rSOH

The third dataset consists of railway ballast stones, which pose the most challenges for the analysis and reconstruction tasks. The acquired meshes are denser, NSS, and can have sharp edges [52] that require higher expansion degrees. The vicinity of sharp edges of the particles requires more points to describe abrupt changes in slope accurately. The harmonic reconstruction of the edges normally requires a higher reconstruction degree than the bulk of the surface. Such surfaces had reconstruction issues with the traditional SH approach and researchers tried to find alternative approaches to overcome these reconstruction challenges [59].

Using the c-rSOH approach, however, we successfully reconstructed all the surfaces with an accurate representation of the sharp edges at a relatively low computational cost (see also Fig. 9). The successful reconstruction requires a combination of choosing the right reconstruction wavelength (related to n_{max}) and a proper reconstruction mesh size to avoid the Gibbs phenomenon. We conducted the c-rSOH analysis using $n_{max} = 40$ and three iterations with the cMCF mapping. For the reconstruction base, we used four refinement cycles of scaled icosahedrons. Fig. 10 shows the reconstruction results of two stones as well as the actual input surface meshes. More reconstruction results for the c-rSOH approach are depicted in Section SI-2.1 of the Supplementary Information for the rest of the dataset stones. The relation between the number of smoothing iterations and the reconstruction error is discussed in Section SI-2.2 of the Supplementary Information.

4.3. Beyond granular mechanics applications

To demonstrate that the presented harmonic decomposition approaches can further be used beyond the intended scope of this paper, a complex visual benchmark was added in Section SI-2.3 of the Supplementary Information. Here we chose to analyze and reconstruct the surface of a Max Planck bust using the c-rSOH approach. In contrast, a c-SH approach (cMCF-preprocessed SH analysis) fails in this example. Consequently, we believe that our proposed SOH reconstruction method has applications beyond granular mechanics, for instance in medical or computer graphics fields [5,60–63].

4.4. Computational cost

Here we briefly discuss the computational cost of the multiple approaches used in the results above. For all methods except c-rSOH, the decomposition (analysis) stage of these spectral methods is by far the most computationally expensive part of the pipeline. Since this part is also identical across these methods, in practice the performance of rSOH, hSOH, and SH is comparable. For further details on the analysis cost, we refer to [44], where direct processing time, memory usage, and scalability for multiple decomposition algorithms were compared.

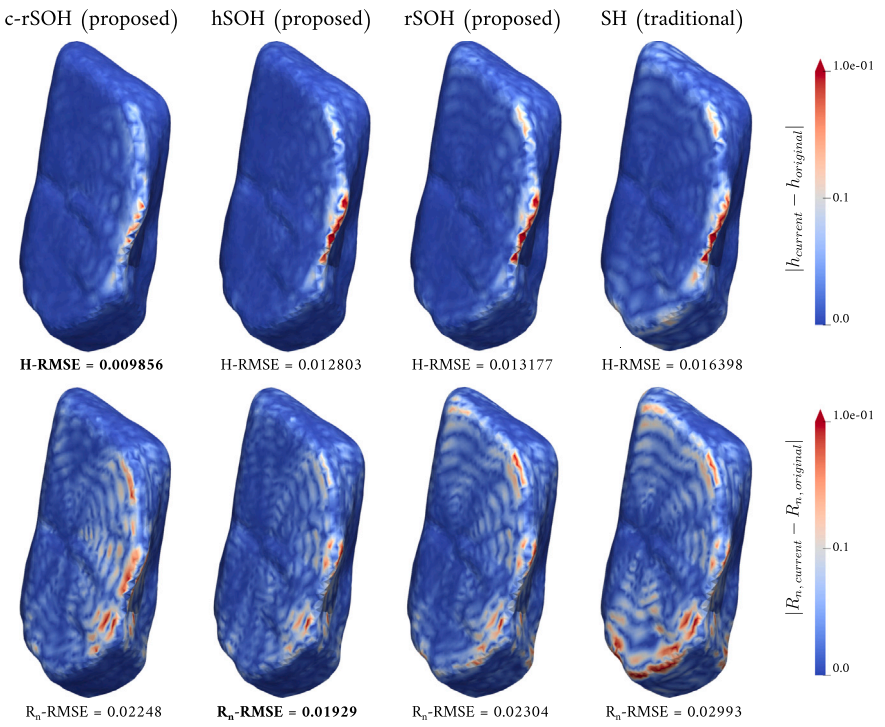

Fig. 9. The local reconstruction error comparison. The upper row shows the absolute difference of the mean curvature (h) for the reconstructed stone B2 [51] using the proposed methods and annotated with the root-mean-square error of the mean curvature (H-RMSE) between the original mean curvature ($h_{original}$) and the currently tested method ($h_{current}$). The lower row shows the same as the upper one but for the local R_n measure and annotated underneath with R_n-RMSE. (For interpretation of the references to color in this figure legend, the reader is referred to the web version of this article.)

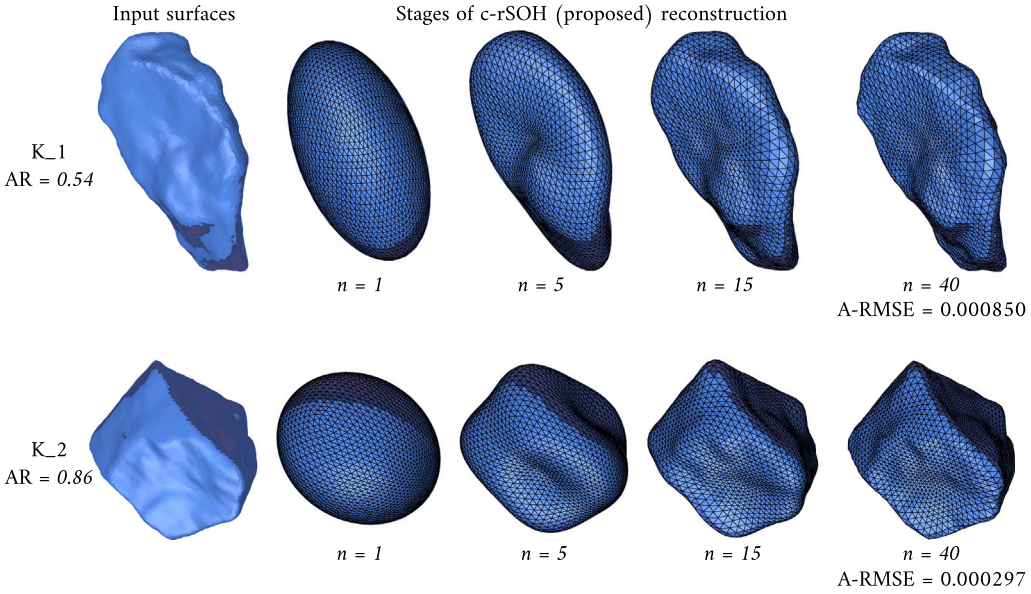

Fig. 10. Reconstruction of a selected set of NSS stones [52] through the c-rSOH approach. The conformal diffeomorphisms were obtained by setting the number of fairing iterations $j = 3$, and we show reconstruction stages up to $n_{max} = 40$ degrees. The final reconstructed stones are annotated (lower right) by the normalized average RMSE (A-RMSE). Intermediate reconstruction stages are also shown for $n \in \{1, 5, 15\}$.

The c-rSOH approach, however, does require increased computational cost compared to the direct mappings. To provide a reference, we time the cost of mapping and analysis for stone B1, which has 2721 vertices and 5438 faces. The timings are done on a laptop computer with an Intel Core i7-11370H CPU, by averaging across three consecutive runs. For this stone, the cMCF algorithm uses three refinement cycles and a step size of 0.0005, and runs on a single CPU core, while the decomposition runs using eight cores in parallel. For this setup, the time taken for cMCF comes to 0.779s; in comparison, the mapping according to rSOH and hSOH took only 14.0 ms. For this stone, the decomposition cost (identical for all methods) using $n_{max} = 30$ required 0.539s. Consequently, the total cost for c-rSOH (i.e. cMCF and decomposition) is more than double the cost for the rSOH and hSOH approaches. Further optimization of the cMCF, e.g. parallelization, could bring this gap down, but the difference between c-rSOH and the other approaches is still substantial.

For the surface of the Max Planck bust (see Section 4.3) with 18872 vertices and 37740 faces the cost of cMCF mapping increased to

5.90600 s using the same previous settings. The decomposition step for $n_{max} = 70$ took 2.6355 min to execute in parallel on eight cores. This indicates that for such high-degree analyses, the decomposition process remains the bottleneck in the pipeline.

5. Conclusions

To study the morphology of closed surfaces, we proposed the spheroidal harmonics (SOH) to generalize the traditional spherical harmonics (SH) approach. Our proposal expands the spherical parameterization domain $\mathbb{S}^2$ into a spheroidal one $\mathcal{E}$ that can be either oblate, prolate, or spherical with arbitrary dimensions for the two semi-major axes (a and c). The newly added degrees of freedom allow for a more flexible parameterization domain that reduces the geometric distortions associated with mapping the particle and avoids the diverging analysis at high expansion degrees, thus, enhancing the analysis and reconstruction quality. This flexible parameterization avoids the use of windowing functions and other techniques that can alter the analysis and shape descriptors. As we use the associated Legendre polynomials and Fourier basis to construct the basis functions, the spheroidal harmonics (SOH) approach is similar to the spherical harmonics (SH). Such similarity will facilitate a seamless integration of this method within existing pipelines.

We proposed three methods for parameterizing closed surfaces onto the spheroidal coordinates. The first method inverts the spheroidal coordinates to achieve a hyperbolic map (hSOH), whose domain is parameterized by the focal distance. The second method uses a rescaled radial-based projection similar to the SH approach (rSOH) so that the aspect ratio is the domain parameter. Between these two methods, the hSOH tends to sample points denser in the vicinity of regions of high curvatures, which has a favorable effect on the reconstruction results compared to rSOH. Moreover, the hSOH was observed to be area-preserving more than the rSOH. Both of these approaches are only valid for SS particles.

Further, we proposed a third approach based on fairing input surfaces conformally, finding smooth diffeomorphism shapes of the input surfaces that can be subsequently mapped onto a spheroid via the radial mapping approach (c-rSOH). To perform fairing we used the conformalized curvature flow (cMCF) approach, which preserves the angles (conformal) of the input manifold. In contrast to rSOH and hSOH, this c-rSOH method works with both SS and NSS particles.

We tested the rSOH, hSOH, and c-rSOH on three datasets and compared the results with the SH. The three proposed SOH-based approaches have successfully reconstructed all the SS particles from the tested datasets, while the traditional SH failed to reconstruct most of these particles without major oscillations. Overall, rSOH and hSOH provide low-cost alternatives to the traditional radial SH harmonics for SS particles, with the hyperbolic mapping method typically outperforming the radial mapping approach. The c-rSOH approach was used to analyze and reconstruct both SS and NSS particles at a small pre-processing computational cost; less than a second of additional computational time for stones of $\mathcal{O}(10^4)$ vertices on a standard laptop. For NSS particles, the c-rSOH is the only method that can perform the analysis; for SS particles the reconstruction quality of the c-rSOH approach is comparable to hSOH. To assess the local reconstruction error of the edges and texture, we measured the difference between the mean curvature measured on the original and reconstructed stones. This error metric indicated that our c-rSOH approach is the best overall approach. However, for the radial-based methods, both rSOH and hSOH scored better than the SH.

The results of the proposed approaches give new avenues for improving the quality of morphology analysis of complex shapes. On the other hand, limitations still exist when considering arbitrary three-dimensional surfaces. For instance, the conformalized mean curvature flow procedure we rely on to tackle NSS surfaces is known to develop pinching singularities for certain types of geometric features and/or a large number of flow iterations. Future research could investigate using rSOH and hSOH mappings in combination with more sophisticated conformal or quasi-conformal mapping techniques, and the associated computational cost increases. Another possible extension of these methods is to combine angle-preserving with area-preserving approaches to obtain more uniformly spaced points on the target spheroidal manifold. Alternatively, a wider range of possible algorithms for the selection of domain parameters for rSOH and hSOH can be proposed to add robustness across a broad range of geometries. Finally, one can extend such approaches to deal with open surfaces as well as surfaces with genus > 0, to help quantify roughness, fractality, and contact detection of simulated granular particles, as well as perform analysis in other physical and medical domains.

Reproducibility

To facilitate the reproducibility of the herein presented results, we made all the Python3.8 codes available online:

- GitHub: https://github.com/msshaqfa/spheroidal-harmonics

We refer readers to the cited datasets for permission reasons, despite having remeshed and cleaned the meshes for analysis.

CRediT authorship contribution statement

Mahmoud Shaqfa: Writing – review & editing, Writing – original draft, Visualization, Validation, Software, Resources, Methodology, Investigation, Funding acquisition, Formal analysis, Data curation, Conceptualization. **Wim M. van Rees:** Writing – review & editing, Writing – original draft, Visualization, Validation, Supervision, Resources, Project administration, Methodology, Investigation, Formal analysis.

Declaration of competing interest

The authors declare the following financial interests/personal relationships which may be considered as potential competing interests: Mahmoud Shaqfa reports financial support was provided by Swiss National Science Foundation. If there are other authors, they declare that they have no known competing financial interests or personal relationships that could have appeared to influence the work reported in this paper.

Acknowledgments

The first author wants to thank the Swiss National Science Foundation (SNSF) for funding this work under project No. P500PT_211088. The authors thank the members of the Earthquake Engineering and Structural Dynamics Laboratory (EESD) at EPFL especially Prof. Katrin Beyer, Dr. Savvas Saloustros, and Andrea Cabriada Ascencio for providing their dataset for the scanned stones. Thanks to Dr. Gary P.T. Choi (The Chinese University of Hong Kong CUHK) for the useful discussions and exchanged conversations.

Appendix A. Supplementary data

Supplementary material related to this article can be found online at https://doi.org/10.1016/j.conbuildmat.2024.138967.

Data availability

Data will be made available on request.

References

[1] S. Wang, Z. Wei, S. Ji, Investigation of the flow characteristics of spherical harmonic particles using the level set method, Powder Technol. 413 (2023) 118069, http://dx.doi.org/10.1016/j.powtec.2022.118069.

[2] M. Shaqfa, K. Beyer, A virtual microstructure generator for 3d stone masonry walls, Eur. J. Mech. A Solids 96 (2022) 104656, http://dx.doi.org/10.1016/j.euromechsol.2022.104656, URL: https://www.sciencedirect.com/science/article/pii/S0997753822001218.

[3] B.D. Zhao, D.H. Wei, J.F. Wang, Particle shape quantification using rotation-invariant spherical harmonic analysis, Geotech. Lett. 7 (2) (2017) 190–196, http://dx.doi.org/10.1680/jgele.17.00011.

[4] C. Brechbühler, G. Gerig, O. Kübler, Parametrization of closed surfaces for 3-D shape description, Comput. Vis. Image Underst. 61 (2) (1995) 154–170.

[5] L. Shen, H. Farid, M.A. McPeek, Modeling three-dimensional morphological structures using spherical harmonics, Evolution 63 (4) (2009) 1003–1016, http://dx.doi.org/10.1111/j.1558-5646.2008.00557.x.

[6] H. Huang, L. Zhang, D. Samaras, L. Shen, R. Zhang, F. Makedon, J. Pearlman, Hemispherical harmonic surface description and applications to medical image analysis, in: Third International Symposium on 3D Data Processing, Visualization, and Transmission, 3DPVT'06, IEEE, 2006, pp. 381–388.

[7] A. Giri, G.P.T. Choi, L. Kumar, Open and closed anatomical surface description via hemispherical area-preserving map, Signal Process. 180 (2021) 107867.

[8] M. Kazhdan, T. Funkhouser, S. Rusinkiewicz, Symmetry descriptors and 3d shape matching, in: Proceedings of the 2004 Eurographics/ACM SIGGRAPH Symposium on Geometry Processing, ACM, 2004, http://dx.doi.org/10.1145/1057432.1057448.

[9] N. Rambaux, V. Lainey, N. Cooper, L. Auzemery, Q.F. Zhang, Spherical harmonic decomposition and interpretation of the shapes of the small saturnian inner moons, Astron. Astrophys. 667 (2022) A78, http://dx.doi.org/10.1051/0004-6361/202243355.

[10] M.A. Wieczorek, M. Meschede, Shtools: Tools for working with spherical harmonics, Geochem. Geophys. Geosyst. 19 (8) (2018) 2574–2592, http://dx.doi.org/10.1029/2018gc007529.

[11] Z. Qian, Multiscale Modeling of Fracture Processes in Cementitious Materials (Ph.D. thesis), 2012, p. 159.

[12] B. Zhou, J. Wang, Generation of a realistic 3d sand assembly using x-ray micro-computed tomography and spherical harmonic-based principal component analysis, Int. J. Numer. Anal. Methods Geomech. 41 (1) (2016) 93–109, http://dx.doi.org/10.1002/nag.2548.

[13] W. Xiong, J. Wang, Gene mutation of particle morphology through spherical harmonic-based principal component analysis, Powder Technol. 386 (2021) 176–192, http://dx.doi.org/10.1016/j.powtec.2021.03.032.

[14] X. Wang, Z. yu Yin, J. qi Zhang, H. Xiong, D. Su, Three-dimensional reconstruction of realistic stone-based materials with controllable stone inclusion geometries, Constr. Build. Mater. 305 (2021) 124240, http://dx.doi.org/10.1016/j.conbuildmat.2021.124240.

[15] B. Zheng, T. Li, H. Qi, L. Gao, X. Liu, L. Yuan, 3D meso-scale simulation of chloride ion transportation in cracked concrete considering aggregate morphology, Constr. Build. Mater. 326 (2022) 126632, http://dx.doi.org/10.1016/j.conbuildmat.2022.126632.

[16] S. Huang, L. Huang, Z. Lai, J. Zhao, Morphology characterization and discrete element modeling of coral sand with intraparticle voids, Eng. Geol. 315 (2023) 107023, http://dx.doi.org/10.1016/j.enggeo.2023.107023.

[17] J. Zhao, S. Zhao, S. Luding, The role of particle shape in computational modelling of granular matter, Nat. Rev. Phys. 5 (9) (2023) 505–525, http://dx.doi.org/10.1038/s42254-023-00617-9.

[18] Y. Hu, J. Li, P. Gao, B. Zhan, Y. Yu, Y. Yang, L. Hong, Q. Yu, Quantification of the residual mortar's distribution and wrapping degree in recycled concrete aggregate based on 3-d reconstruction technology, Constr. Build. Mater. 414 (2024) 134983, http://dx.doi.org/10.1016/j.conbuildmat.2024.134983.

[19] A. Paixão, E. Fortunato, Abrasion evolution of steel furnace slag aggregate for railway ballast: 3d morphology analysis of scanned particles by close-range photogrammetry, Constr. Build. Mater. 267 (2021) 121225, http://dx.doi.org/10.1016/j.conbuildmat.2020.121225.

[20] M. Imaran, J. Young, R. Capozza, K. Stratford, K.J. Hanley, Spherical harmonic–based dem in lammps: Implementation, verification and performance assessment, Comput. Phys. Comm. 304 (2024) 109290, http://dx.doi.org/10.1016/j.cpc.2024.109290.

[21] A. Jacobson, D. Panozzo, et al., libigl: A simple C++ geometry processing library, 2018, https://libigl.github.io/.

[22] H. Wadell, Volume, shape, and roundness of rock particles, J. Geol. 40 (5) (1932) 443–451, http://dx.doi.org/10.1086/623964.

[23] A. Gelb, The resolution of the gibbs phenomenon for spherical harmonics, Math. Comp. 66 (218) (1997) 699–717, URL: http://www.jstor.org/stable/2153890.

[24] M.K. Chung, K.M. Dalton, L. Shen, A.C. Evans, R.J. Davidson, Weighted fourier series representation and its application to quantifying the amount of gray matter, IEEE Trans. Med. Imaging 26 (4) (2007) 566–581, http://dx.doi.org/10.1109/tmi.2007.892519.

[25] K. Khairy, J. Howard, Spherical harmonics-based parametric deconvolution of 3d surface images using bending energy minimization, Med. Image Anal. 12 (2) (2008) 217–227, http://dx.doi.org/10.1016/j.media.2007.10.005.

[26] G.P.T. Choi, K.T. Ho, L.M. Lui, Spherical conformal parameterization of genus-0 point clouds for meshing, SIAM J. Imaging Sci. 9 (4) (2016) 1582–1618, http://dx.doi.org/10.1137/15m1037561.

[27] M.H. Yueh, W.W. Lin, C.T. Wu, S.T. Yau, An efficient energy minimization for conformal parameterizations, J. Sci. Comput. 73 (1) (2017) 203–227, http://dx.doi.org/10.1007/s10915-017-0414-y.

[28] G.P.T. Choi, Y. Leung-Liu, X. Gu, L.M. Lui, Parallelizable global conformal parameterization of simply-connected surfaces via partial welding, SIAM J. Imaging Sci. 13 (3) (2020) 1049–1083.

[29] M. Jin, J. Kim, F. Luo, X. Gu, Discrete surface ricci flow, IEEE Trans. Vis. Comput. Graphics 14 (5) (2008) 1030–1043, http://dx.doi.org/10.1109/tvcg.2008.57.

[30] M. Kazhdan, J. Solomon, M. Ben-Chen, Can mean-curvature flow be modified to be non-singular? Comput. Graph. Forum 31 (5) (2012) 1745–1754, http://dx.doi.org/10.1111/j.1467-8659.2012.03179.x.

[31] K. Crane, U. Pinkall, P. Schröder, Robust fairing via conformal curvature flow, ACM Trans. Graph. 32 (4) (2013) 1–10, http://dx.doi.org/10.1145/2461912.2461986.

[32] J.D. McEwen, Y. Wiaux, A novel sampling theorem on the sphere, IEEE Trans. Signal Process. 59 (12) (2011) 5876–5887, http://dx.doi.org/10.1109/tsp.2011.2166394.

[33] S. Nadeem, Z. Su, W. Zeng, A. Kaufman, X. Gu, Spherical parameterization balancing angle and area distortions, IEEE Trans. Vis. Comput. Graphics 23 (6) (2017) 1663–1676, http://dx.doi.org/10.1109/tvcg.2016.2542073.

[34] A. Giri, G.P.T. Choi, L. Kumar, Open and closed anatomical surface description via hemispherical area-preserving map, Signal Process. 180 (2021) 107867.

[35] M. Shaqfa, G.P.T. Choi, K. Beyer, Spherical cap harmonic analysis (SCHA) for characterising the morphology of rough surface patches, Powder Technol. 393 (2021) 837–856, http://dx.doi.org/10.1016/j.powtec.2021.07.081, URL: https://www.sciencedirect.com/science/article/pii/S0032591021006720.

[36] M. Shaqfa, G.P. Choi, G. Anciaux, K. Beyer, Disk harmonics for analysing curved and flat self-affine rough surfaces and the topological reconstruction of open surfaces, 2024, Submitted.

[37] Z.Y. Zhou, R.P. Zou, D. Pinson, A.B. Yu, Dynamic simulation of the packing of ellipsoidal particles, Ind. Eng. Chem. Res. 50 (16) (2011) 9787–9798, http://dx.doi.org/10.1021/ie200862n.

[38] Z. Zhu, H. Chen, Aggregate shape effect on the overestimation of interface thickness for spheroidal particles, Powder Technol. 313 (2017) 218–230, http://dx.doi.org/10.1016/j.powtec.2017.03.014.

[39] W.E. Byerly, An Elementary Treatise on Fourier's Series and Spherical, Cylindrical, and Ellipsoidal Harmonics: With Applications To Problems in Mathematical Physics, Ginn and Company, 1893.

[40] W. Smythe, Static and Dynamic Electricity. International Series in Pure and Applied Physics, McGraw-Hill, 1950.

[41] P.M. Morse, H. Feshbach, Methods of theoretical physics, 1953.

[42] M. Abramowitz, I.A. Stegun, Handbook of Mathematical Functions with Formulas, Graphs, and Mathematical Tables. Ninth Dover Printing, Tenth Gpo Printing Ed., Dover, New York, 1964.

[43] P. Moon, D.E. Spencer, Field Theory Handbook, Springer Berlin Heidelberg, 1988, http://dx.doi.org/10.1007/978-3-642-83243-7.

[44] M. Shaqfa, K.R. dos Santos, K. Beyer, On the conjugate symmetry and sparsity of the harmonic decomposition of parametric surfaces with the randomised kaczmarz method, Signal Process. (2024) 109462, http://dx.doi.org/10.1016/j.sigpro.2024.109462, URL: https://www.sciencedirect.com/science/article/pii/S0165168424000811.

[45] M. Kazhdan, J. Solomon, M. Ben-Chen, Can mean-curvature flow be made non-singular? in: Eurographics Symposium on Geometry Processing, Vol. 2012, 2012, http://dx.doi.org/10.48550/ARXIV.1203.6819, URL: https://arxiv.org/abs/1203.6819.

[46] S. Saloustros, A. Settimi, A. Cabriada Ascencio, J. Gamerro, Y. Weinand, K. Beyer, Dataset for geometrical digital twins of the as-built microstructure of three-leaf stone masonry walls with laser scanning, 2023, http://dx.doi.org/10.5281/ZENODO.7093710, URL: https://zenodo.org/record/7093710.

[47] G. Huisken, Flow by mean curvature of convex surfaces into spheres, J. Differential Geom. 20 (1) (1984) http://dx.doi.org/10.4310/jdg/1214438998.

[48] M. Meyer, M. Desbrun, P. Schröder, A.H. Barr, Discrete differential-geometry operators for triangulated 2-manifolds, in: Mathematics and Visualization, Springer Berlin Heidelberg, 2003, pp. 35–57, http://dx.doi.org/10.1007/978-3-662-05105-4_2.

[49] S. Saloustros, A. Settimi, A.C. Ascencio, J. Gamerro, Y. Weinand, K. Beyer, Geometrical digital twins of the as-built microstructure of three-leaf stone masonry walls with laser scanning, Sci. Data 10 (1) (2023) http://dx.doi.org/10.1038/s41597-023-02417-3.

[50] P.S.M. Thilakarathna, S.K. Baduge, P. Mendis, E.R.K. Chandrathilaka, V. Vimonsatit, H. Lee, Aggregate geometry generation method using a structured light 3D scanner, spherical harmonics–based geometry reconstruction, and placing algorithms for mesoscale modeling of concrete, J. Mater. Civ. Eng. 33 (8) (2021) http://dx.doi.org/10.1061/(asce)mt.1943-5533.0003851.

[51] S. Thilakarathna, 3D scanned aggregates, 2020, http://dx.doi.org/10.17632/X5DBX8YXDW.1, URL: https://data.mendeley.com/datasets/x5dbx8yxdw/1.
[52] B. Suhr, W.A. Skipper, R. Lewis, K. Six, Shape analysis of railway ballast stones: curvature-based calculation of particle angularity, Sci. Rep. 10 (1) (2020) http://dx.doi.org/10.1038/s41598-020-62827-w.
[53] B. Suhr, K. Six, W.A. Skipper, R. Lewis, 3D scans of two types of railway ballast including shape analysis information, 2020, http://dx.doi.org/10.5281/ZENODO.3689592, URL: https://zenodo.org/record/3689592.
[54] M. Kazhdan, H. Hoppe, Screened Poisson surface reconstruction, ACM Trans. Graph. 32 (3) (2013) 1–13, http://dx.doi.org/10.1145/2487228.2487237.
[55] P. Cignoni, M. Callieri, M. Corsini, M. Dellepiane, F. Ganovelli, G. Ranzuglia, Meshlab: an open-source mesh processing tool, in: Eurographics Italian Chapter Conference, Salerno, Italy, Vol. 2008, 2008, pp. 129–136.
[56] C. Lawson, Software for c1 surface interpolation, in: J.R. Rice (Ed.), Mathematical Software, Academic Press, 1977, pp. 161–194, http://dx.doi.org/10.1016/B978-0-12-587260-7.50011-X, URL: https://www.sciencedirect.com/science/article/pii/B978012587260750011X.
[57] D. Panozzo, E. Puppo, L. Rocca, Efficient multi-scale curvature and crease estimation, 2010, URL: https://api.semanticscholar.org/CorpusID:17213450.
[58] J.W. Bullard, E.J. Garboczi, Defining shape measures for 3d star-shaped particles: Sphericity, roundness, and dimensions, Powder Technol. 249 (2013) 241–252, http://dx.doi.org/10.1016/j.powtec.2013.08.015.
[59] N. Ouhbi, C. Voivret, G. Perrin, J.N. Roux, 3D particle shape modelling and optimization through proper orthogonal decomposition, Granul. Matter 19 (4) (2017) http://dx.doi.org/10.1007/s10035-017-0771-0.
[60] H. Huang, L. Shen, R. Zhang, F. Makedon, B. Hettleman, J. Pearlman, Surface Alignment of 3D Spherical Harmonic Models: Application To Cardiac MRI Analysis, Springer Berlin Heidelberg, pp. 67–74, http://dx.doi.org/10.1007/11566465_9.
[61] M. Styner, I. Oguz, S. Xu, C. Brechbühler, D. Pantazis, J.J. Levitt, M.E. Shenton, G. Gerig, Framework for the statistical shape analysis of brain structures using spharm-pdm, Insight J. 1071 (2006) 242–250, URL: https://api.semanticscholar.org/CorpusID:6706349.
[62] A. Medyukhina, M. Blickensdorf, Z. Cseresnyés, N. Ruef, J.V. Stein, M.T. Figge, Dynamic spherical harmonics approach for shape classification of migrating cells, Sci. Rep. 10 (1) (2020) http://dx.doi.org/10.1038/s41598-020-62997-7.
[63] J. Grieb, I. Barbero-García, J.L. Lerma, Spherical harmonics to quantify cranial asymmetry in deformational plagiocephaly, Sci. Rep. 12 (1) (2022) http://dx.doi.org/10.1038/s41598-021-04181-z.